Control of Emission Characteristics of Perovskite Lasers through Optical Feedback

Alexander Palatnik,* Changsoon Cho, Chonghe Zhang, Markas Sudzius, Martin Kroll, Stefan Meister, and Karl Leo*

Recent progress on perovskite lasers has shown the large potential for such materials to become a basis for commercially available microlasers in the near feature. Herein, distributed feedback (DFB) lasers based on vacuum-processed CsPbBr₃ are investigated. The expansion of the DFB structure from 1D to 2D suppresses parasitic amplified spontaneous emission (ASE), resulting in the multiple-time-enhanced lasing output. Further, the photoluminescence and lasing behavior of 1D and 2D DFB structures are explored through the *k*-space imaging analysis.

1. Introduction

Metal halide perovskites are under extensive research as candidates for light-harvesting and light-emitting devices. Impressive results have already been achieved using such perovskites as solar cells,[1] reaching power conversion efficiency of over 25%,[2,3] due to high absorption coefficients, long charge carrier diffusion lengths, and well-suited direct bandgap of relevant perovskites. Their properties such as low trap density and high luminescence efficiency also resulted in bright perovskite light-emitting diodes (LEDs)[4] as a source of electroluminescence, exceeding quantum efficiency of 20%.[5–7] Perovskite-based lasers have been demonstrated in various cavity configurations and material morphologies.[8–11] Recently, the optically pumped lasing threshold at room temperature was reduced, allowing continuous wave (CW) lasing,[12–15] which is an important intermediate step toward the goal of electrically pumped lasers.[16,17]

Lasing has been demonstrated using many different perovskite compositions and preparation methods.[8–10,12,18,19–33] While the hybrid perovskites are more studied and possibly show lower

thresholds, inorganic perovskites show better thermal stability and lifetimes.[34–37] Among the optical configurations used in perovskite-based lasers are planar microcavities,[33] nanowires,[20,28] spherical resonators,[9,19,30] whispering gallery mode resonators,[8,18] nanocuboids,[38] distributed feedback (DFB) lasers,[10,12,14,24,25,27,29,32] and 2D structures.[21–23,26] Among those schemes, DFB lasers have attracted attention due to resonance controllability by optimizing the grating period. Moreover, unlike other complicated structures, the DFB can be directly implemented to planar thin films by structuring the bottom layer or nanoimprinting the top surface. It is believed to be the most compatible resonator with conventional thin-film diode structures, as shown by recent works.[39,40] However, compared with the intensive research effort on material engineering for perovskite lasers, the optical aspects of DFB lasers have not been deeply investigated, mainly due to the short history of research. Moreover, while current research efforts are mostly focusing on the reduction of lasing threshold, to get closer to electrically pumped devices, the efficiency of lasing output has not been sufficiently optimized, leaving room for exploration.

Based on thermally evaporated CsPbBr₃ perovskites, here, we investigate 1D and 2D DFB lasers to obtain better understanding of their design rules. While both lasers achieve low lasing thresholds compared with thresholds of amplified spontaneous emission (ASE) of a pure film, the 2D DFB lasers are shown to reach a higher lasing output power by suppressing the loss pathway of ASE. We conduct a detailed mode analysis in *k*-space, to describe the optical properties of 1D and 2D DFB structures and provide further insight for future perovskite lasers.

A. Palatnik, C. Cho, C. Zhang, M. Sudzius, M. Kroll, S. Meister, K. Leo
Dresden Integrated Center for Applied Physics and Photonic Materials
Technische Universität Dresden
Dresden 01062, Germany
E-mail: alexander.palatnik@tu-dresden.de; karl.leo@tu-dresden.de
C. Cho
Cavendish Laboratory, Department of Physics
University of Cambridge
J.J. Thomson Avenue, Cambridge CB3 0HE, UK

2. Results and Discussion

First, we examine the photoluminescence (PL) of the CsPbBr₃ perovskite as an unstructured layer and on top of 1D and 2D DFB structures (**Figure 1**a,c,d). The X-ray diffraction analysis (XRD) of the unstructured perovskite layer shows a tetragonal crystalline phase (Figure 1b) and photoluminescence quantum yield (PLQY) of 0.018%. PL of an unstructured layer excited by pulsed laser (wavelength of 400 nm and durations of 100 fs and 1 ns) shows ASE at $30 \pm 2\,\mu J\,cm^{-2}$ (**Figure 2**a,b). While a few works reported dependence of the ASE threshold on the duration of the excitation pulse,[11] here, the ASE thresholds at 100 fs and 1 ns pulses are shown to be almost identical. This indicates that charge recombination lifetime near the threshold condition
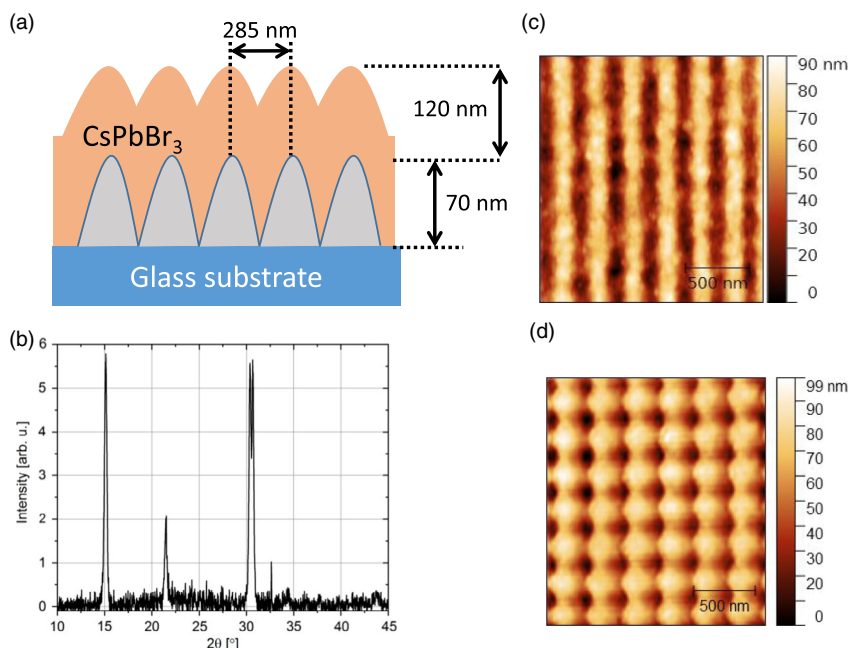
Figure 1. a) Schematics of the DFB device. Corrugated structure on the glass substrate with perovskite layer evaporated on top. b) XRD analysis of the unstructured perovskite layer shows a tetragonal crystalline phase. c,d) Atomic force microscope (AFM) scan of the corrugated layer of the 1D and 2D DFB accordingly.
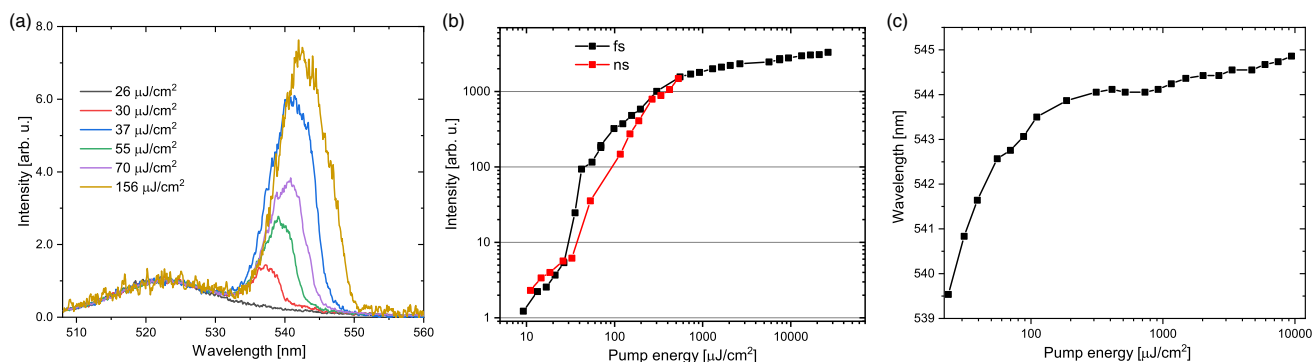

Figure 2. Emission of the unstructured layer of the perovskite under an optical excitation. a) Emission spectrum of the perovskite below and above ASE threshold. b) Input–output curve for ASE emission for femtosecond (100 fs) and nanosecond (1 ns) excitation. c) Dependence of the peak position of the ASE on the pump energy.

in the perovskite is longer than 1 ns and hence depletion of population inversion during the pump pulse is not significant.

Further increasing pump energy leads to a shift of the ASE emission peak away from absorption region toward longer wavelengths from 537 to 545 nm, as well as the broadening of the spectral shape (Figure 2a,c). It is consistent with previous reports on ASE of $CsPbBr_3$, whereas their origin is still under debate.[41–44] Output intensity saturation is observed for pump intensities above $1000\,\mu J\,cm^{-2}$ (Figure 2b).

To fabricate DFB lasers, we prepare 1D and 2D grating structures with a period of 285 nm, aiming for resonance at wavelength of 540 nm (refer to the Experimental Section for details). The $CsPbBr_3$ perovskite layers (120 nm) are formed by thermally coevaporating CsBr and $PbBr_2$ precursors on the structured substrates. The evaporation process enables the

perovskite layer to conformally follow the structure, as shown in Figure 1a. Lasing in both DFB samples is observed at threshold of $13 \pm 3\,\mu J\,cm^{-2}$ (**Figure 3**a), regardless of the pump pulse duration, as explained earlier. The emission above the lasing threshold is spectrally narrow (full width at half maximum (FWHM) of 0.5 nm), polarized, and directed. All samples exhibit high stability under excitation and show steady output for pump intensities up to $10^4\,E_{th}$, where E_{th} is the threshold energy density.

Introduction of a small thickness gradient in perovskite layers allows tunability of the resonances in the range of about 10 nm due to changes in the effective refractive index of the waveguides. We observed the same values of the threshold within the error range for both structures and all wavelengths under consideration, contrary to previous work, showing reduced thresholds for 2D DFB in nonperovskite emitters.[45,46] In contrast, 2D
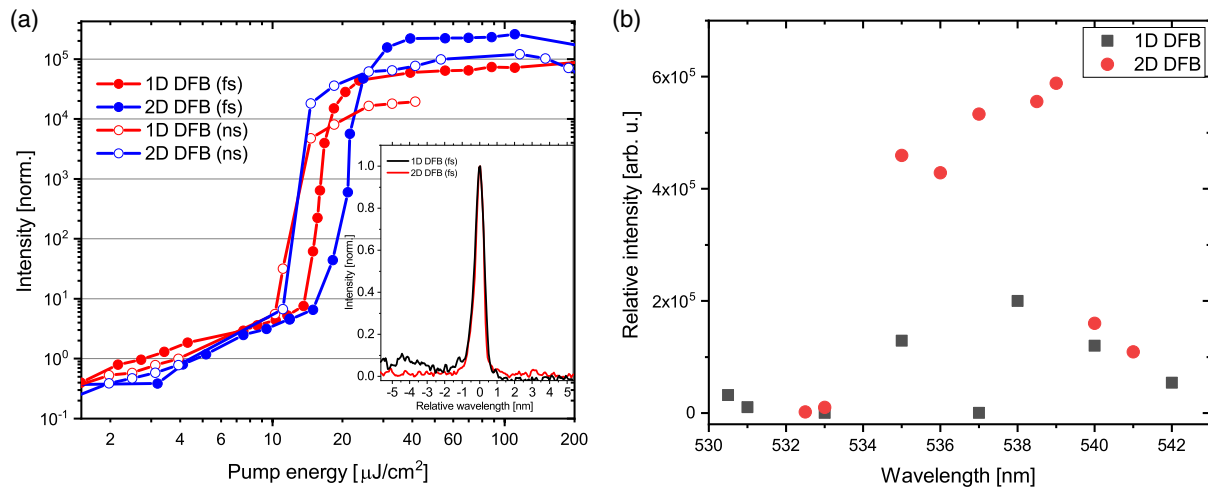
Figure 3. a) Input–output curves for 1D and 2D DFB lasers for femtosecond (100 fs) and nanosecond (1 ns) excitations, whereas the output intensities were measured at lasing wavelengths (inset: normalized spectrum above the lasing threshold). b) Dependence of the lasing output at saturation on wavelengths for 1D and 2D DFB structures. The relative intensity represents maximal lasing output normalized by PL at threshold for best devices and different wavelengths.

DFB lasers reach saturation at higher levels of output, allowing more efficient light extraction. In Figure 2b, we compare lasing output normalized by PL at threshold for best-performing devices at different wavelengths, representing maximal amplification achieved. The region of the highest output is 534–540 nm, which is within the ASE range, but has a shorter wavelength than the ASE peak at high pump intensities (Figure 2c). We observe device-to-device variations for all the samples, yet the 2D DFB devices systematically provide higher outputs compared with 1D DFB by a factor of 3 and more. Most 2D DFB devices perform very close to the shown best results; however, variations of output power for 1D DFB are much larger. We attribute the higher sensitivity of 1D devices to fabrication imperfections. For the best devices, we observe a total output above 4 nJ for 2D DFB and 0.75 nJ for 1D DFB in the lasing regime. Both are observed at the onset of saturation at about $50\,\mu Jcm^2$ and up to $10000\,\mu Jcm^2$ without noticeable change in output intensity.

The far-field emission patterns and the mode structure of 1D DFB devices can be understood from the sketch shown in **Figure 4**a, which schematically represents scattering and coupling of light in the k-space.[47] Depicted circles correspond to a mode at a fixed wavelength and are centered at around $-2\pi\Lambda$, 0, and $2\pi\Lambda$, where Λ is the grating periodicity. The radius of each circle is n_{eff}/λ, where n_{eff} is the effective refractive index of the waveguide and λ is the wavelength of the propagating mode. The shaded area around the origin of coordinates schematically represents k_x and k_y, which lie inside of the light escape cone and hence can be outcoupled from the waveguide. The coupling between different modes occurs on intersection points between the circles. Coupling of two counterpropagating modes in the origin of the coordinates ($k_x = k_y = 0$) provides a mechanism for an effective optical feedback, which can lead to lasing in favourable conditions.

We carry out a direct measurement of the wavelength dependence on in-plane momentum, k. Using a polarization analyzer,

we separate transverse electric (TE) (**Figure 5**a,b) and transverse magnetic (TM) (Figure 5c,d) modes. In this figure, for both TE and TM, the intersections of modes in $k_\perp = 0$ are visible; however, it lies outside the high-gain spectral region and, therefore, no lasing should be expected in these particular samples. For higher pump energies, we observe ASE (Figure 5b,d), which sometimes can be misinterpreted as lasing if only the spectrum is considered but can be unambiguously identified in k-space as no directional emission is observed above the threshold.

The mode structure of 2D DFB can be understood as a superposition of two perpendicular 1D structures in k-space (Figure 4b). To get further insight into the mode structure, we conduct 1D cuts of 2D k-space (**Figure 6**). To make all modes visible, we slightly tilt the sample and introduce a small detuning from $k_y = 0$. In Figure 6a, TE_x modes are clearly visible, whereas TE_y modes cannot be seen directly (as they are p-polarized), but can be seen through their interaction with the TE_x mode. All the modes intersect at the vicinity of $k_x = k_y = 0$, providing coupling, which can lead to lasing in the normal direction. For $k_y \neq 0$ (Figure 6b) cut, only a slight change is seen in the TE_x mode, but now the TM_y mode is clearly visible. For p-polarized emission (Figure 6c), interaction between TM_x and TE_y can be seen. Figure 6d shows the interaction between TM_x and TM_y modes for $k_y \neq 0$ cut. The TM_y mode is not directly visible but can be deduced through points of more intense emission. **Figure 7** shows schematically the discussed cuts in the k-space. We mark momentum coordinates where lasing occurs by red spots and show green dashed lines for measured k-space cuts. Such a diagram represents a single fixed-wavelength slice, whereas in principle lasing can occur simultaneously at other wavelengths too and should be described by diagrams with circles of different radii.

When the gain is high enough, the above-described interaction of modes leads to lasing. To illustrate it, we superimpose two k-space images of lasing (lasing at normal direction and
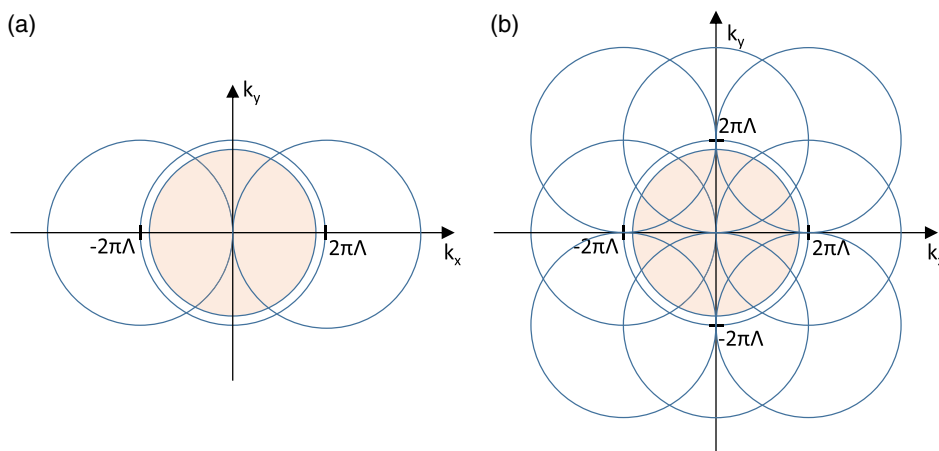
Figure 4. Schematics of the mode structure in the *k*-space. a) Circles are centered around $-2\pi\Lambda$, 0, and $2\pi\Lambda$ and represent a mode at a fixed wavelength of 1D DFB. The shaded area represents k_x and k_y, which lie inside the light escape cone. b) 2D DFB structure is a superposition of two 1D DFB structures along k_x and k_y axes.
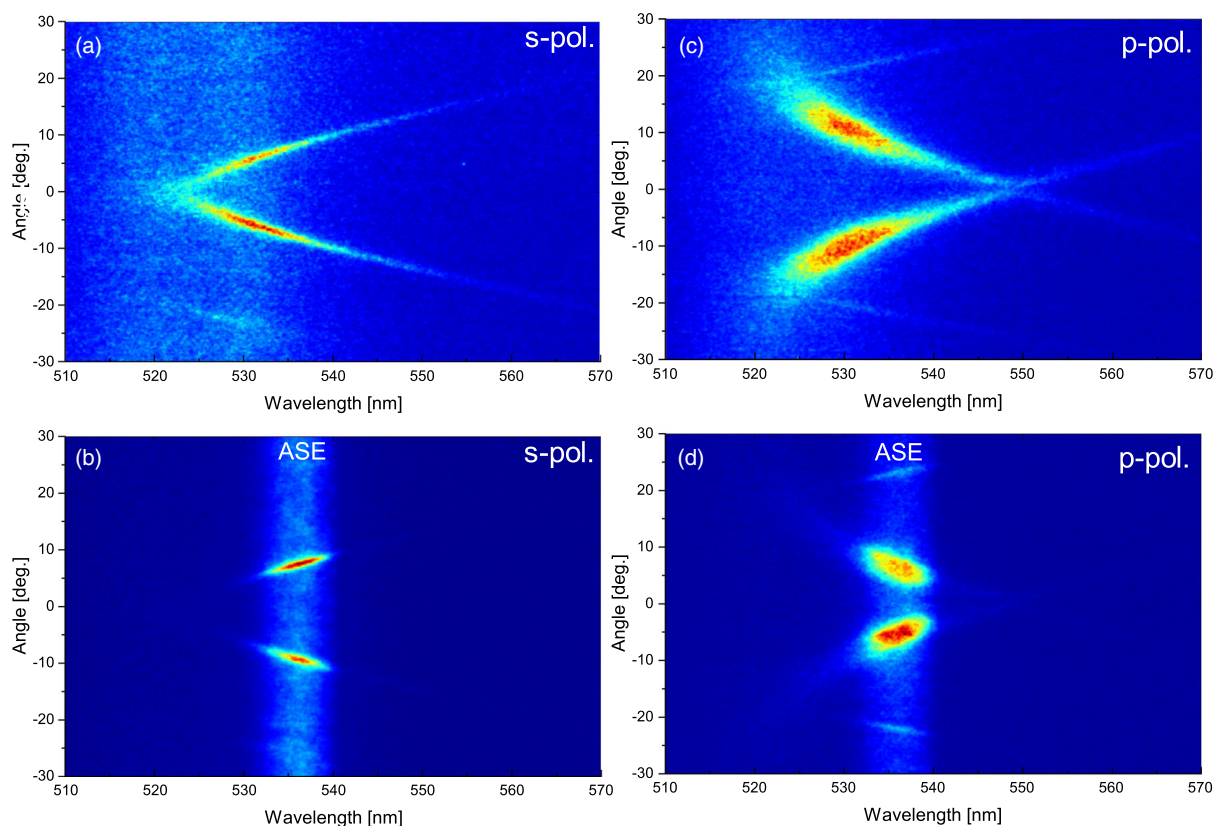

Figure 5. Images of 1D DFB structures in the *k*-space. a) s-polarized emission below ASE threshold (TE mode). b) s-polarized emission above ASE threshold (TE mode). c) p-polarized emission below ASE threshold (TM mode). d) p-polarization emission above ASE thershold (TM mode).

at angle) on the *k*-space-mode image (**Figure 8**a,b for 1D and 2D structures). In the far field, we observe a standard pattern of emission from 1D DFB structures (Figure 8c,d).[24,48] Arcs on the image correspond to alternating TE and TM modes (starting from TE mode in the center), propagating in opposite directions. The far-field image is a full *k*-space projection; therefore arcs are

parts of the circles lying within the light cone (Figure 7a). For 2D DFB structures, the far-field lasing pattern shows a center spot and four arms of the cross (Figure 8e). The center spot has a ring shape (cannot be resolved in the image), which can be attributed to 2D Bloch modes,[26] whereas arms are other intersections of momentum circles, as was discussed before.
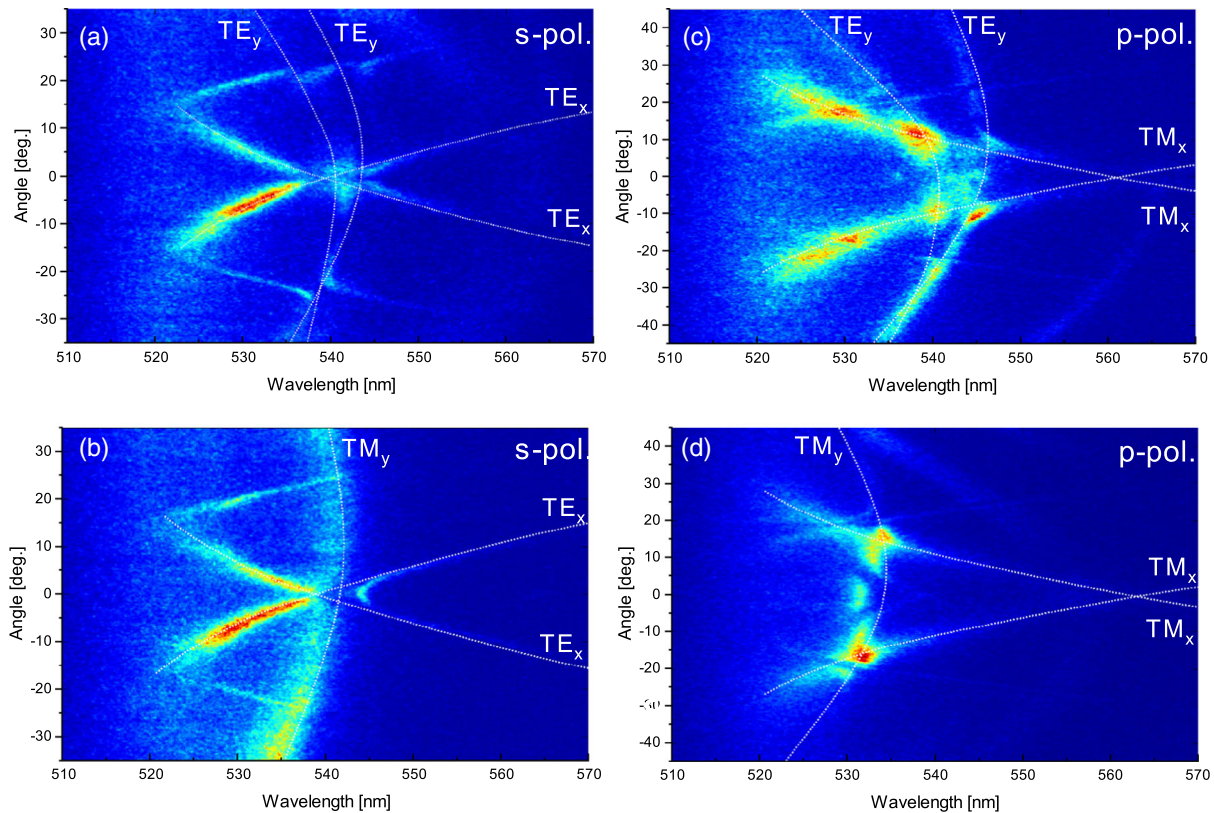
Figure 6. Images of 2D DFB structures in the *k*-space. a) s-polarized emission for $k_x = 0$ and $k_y \approx 0$. b) s-polarized emission for $k_x = 0$ and $k_y \neq 0$. c) p-polarized emission for $k_x = 0$ and $k_y \approx 0$. d) p-polarized emission for $k_x = 0$ and $k_y \neq 0$.
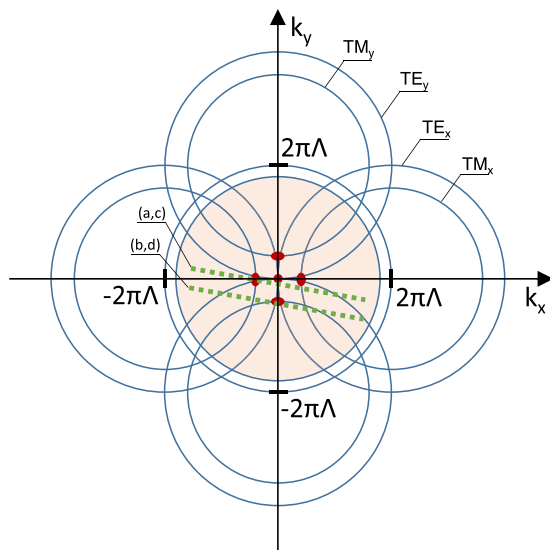

Figure 7. Schematics of 2D DFB mode structure in the *k*-space. Red dots are points in *k*-space, where lasing occurs. Green dashed lines are experimentally measured 1D cuts.

The *k*-space imaging of the device emission allows us to suggest an explanation for the difference between saturation levels of 1D and 2D devices. Careful comparison of the *k*-space-resolved emission spectra of 1D and 2D DFB structures reveals an ASE

along with lasing emission (**Figure 9**a,b) in 1D structures. While lasing can be seen as localized bright spots, which correspond to narrow linewidth and directional emission, broader and undirected ASE is seen as vertical stripes (similar to Figure 5b,d). We do not observe such effects for 2D structures, where light is confined in both directions (Figure 9c,d). It is well known that in macroscopic lasers, ASE is undesirable and leads to lower emission saturation, and therefore laser systems are designed in a way to minimize it. In microscopic lasers, due to the small volume of active material and higher *β*-factors, ASE is rarely observed together with lasing. However, the low ASE threshold in perovskite materials can have a negative influence on lasing at high pump rates. In fact, in our devices, ASE and lasing have similar thresholds and we observe their coexistence for 1D structures.

3. Conclusion

In this work, we investigate emission and lasing of thermally evaporated CsPbBr$_3$ perovskite formed on top of 1D and 2D DFB structures. We analyzed mode structures, far-field patterns, and lasing thresholds and output for both cases. Furthermore, we assess not only the lasing threshold, but also the output emission at high pump rates, which is influenced by emission saturation effects in perovskite, as well as by specific feedback structures. We find that the 2D DFB structures are superior to 1D DFB
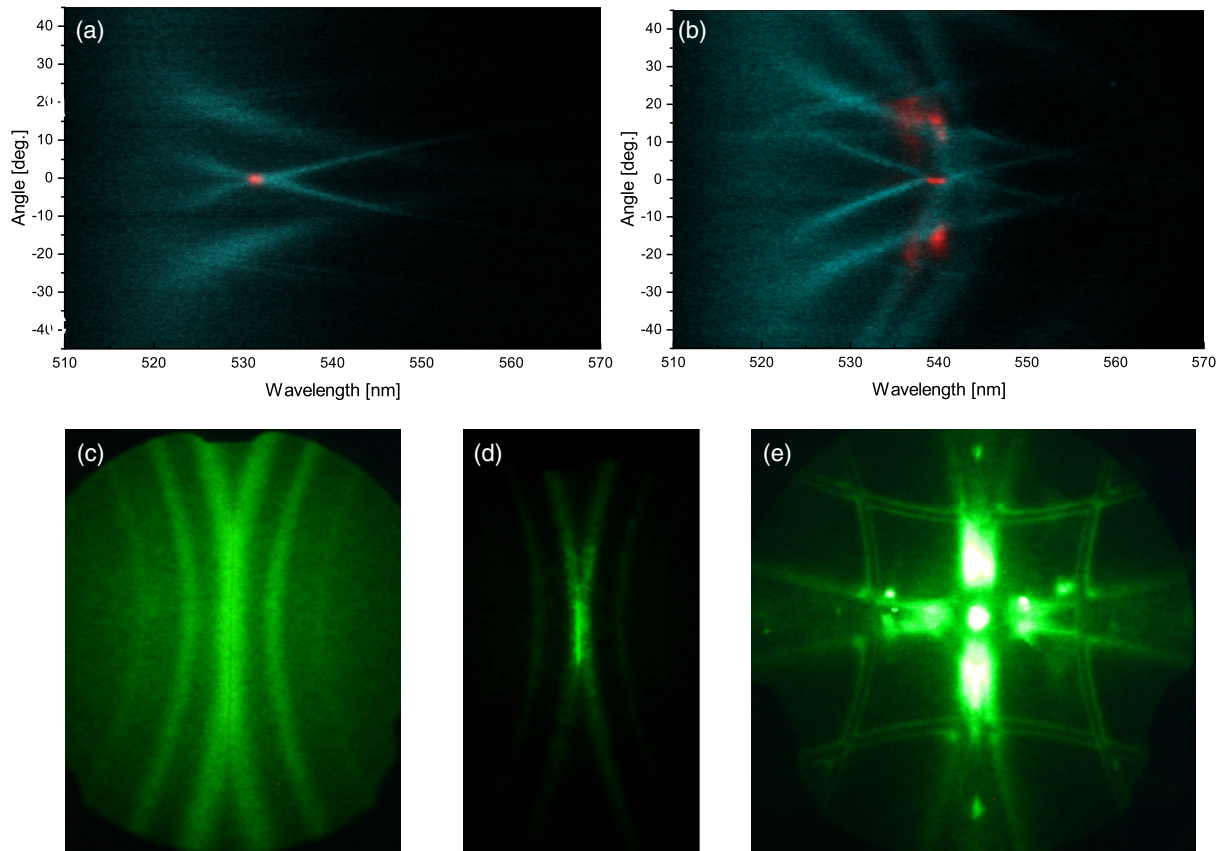
Figure 8. a) Lasing in 1D DFB (red) superimposed on PL (cyan). b) Lasing in 2D DFB (red) superimposed on PL (cyan). c) Far-field image of PL from 1D DFB below the threshold. d) Far-field emission from 1D DFB just above the threshold. e) Far-field emission from 2D DFB just above the threshold.
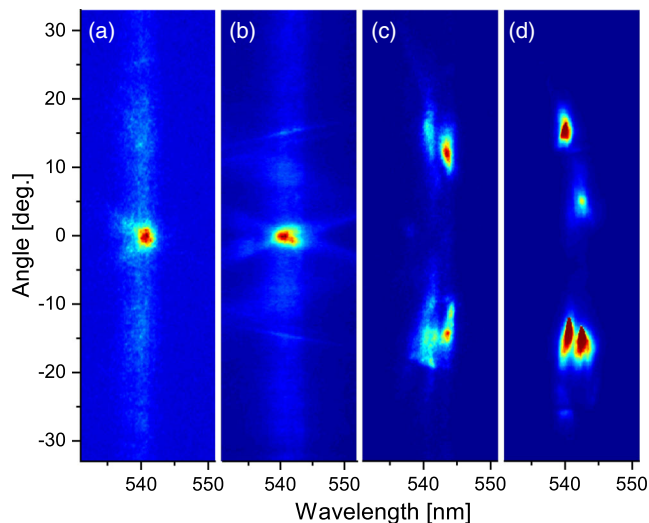

Figure 9. Examples of lasing in *k*-space when the pump intensity exceeds ASE threshold. a,b) Examples of coexistence of lasing and ASE in 1D DFB just above the ASE threshold at the different spots of the identical devices, showing the repeatability of the result. c,d) Examples of emission from 2D DFB above ASE threshold at the different spots of the identical devices.

and produce stronger output at saturation excitation. We attribute this to the better mode confinement in such structures

and suppression of the competition between ASE and lasing. We believe that emission saturation and the possible negative influence of ASE in perovskites should be taken into account in the development of high-output-power perovskite lasers.

4. Experimental Section

Fabrication of DFB Structure: The Bragg condition for wavelength λ was satisfied when $N\lambda = 2n_{eff}\Lambda$, where N is the grating order ($N = 2$ for second-order grating, which is used in this work), Λ is gating periodicity, and n_{eff} is the effective refractive index of the waveguide which is numerically solved[49] for the grating depth of 70 nm and perovskite layer of 120 nm to obtain $\Lambda = 285$ nm. To fabricate the structure, we used negative photoresist AZ nLOF 2020. The photoresist was deposited by spin coating on a glass substrate and exposed to the interference of UV laser light using Lloyd's mirrors configuration; however, by adjusting the mirror angle, the grating period was tuned to 285 nm. For 2D structures, the sample was rotated by 90° and exposed again.

Perovskite Deposition: A 120 nm-thick $CsPbBr_3$ was thermally evaporated on top of structures. The $CsPbBr_3$ layers were deposited by coevaporation of CsBr (Sigma) and PbBr (Sigma) in a vacuum deposition chamber (MINI PEROvap, CreaPhys GmbH, Germany) at a base pressure of 2e-6 mbar. Slight thickness gradient naturally appeared on large-area samples, allowing device tunability.

The deposition rates were monitored with separate quarz crystal balances and held constant at a deposition rate of 0.11 A s^{-1} for CsBr and 0.13 A s^{-1} for PbBr. The high refractive index of the perovskite ($n \approx 2.1$)[44] situated between air and photoresist ($n \approx 1.5$) provided a waveguide.

Characterization of Lasing Properties: The sample was excited by femtosecond laser pulses with a duration of 100 fs and repetition rate of 5 KHz. The pulses were produced with a Micra femtosecond oscillator and amplified with a regenerative amplifier (RA) Legend Elite Duo, both by Coherent. The second harmonic was generated at 400 nm from the output of the RA. The same setup was used to produce nanosecond pulses by bypassing the compression stage of the RA. Excitation beam was focused by a lens to a spot size of 120 μm in diameter. The emission was collected by high numerical aperture (NA) objective lens and guided into a spectrometer, equipped with a cooled charge coupled device (CCD) camera. For *k*-space imaging, we used additional pair of lenses to image back the focal plan of the objective lens onto the spectrometer entrance slit.[50]

Conflict of Interest

The authors declare no conflict of interest.

Data Availability Statement

Research data are not shared.

[1] A. Kojima, K. Teshima, Y. Shirai, T. Miyasaka, *J. Am. Chem. Soc.* **2009**, *131*, 6050.

[2] *Cell efficiency chart*, https://www.nrel.gov/pv/cell-efficiency.html (accessed: April **2021**).

[3] J. J. Yoo, G. Seo, M. R. Chua, T. G. Park, Y. Lu, F. Rotermund, Y.-K. Kim, C. S. Moon, N. J. Jeon, J.-P. Correa-Baena, V. Bulović, S. Sik Shin, M. G. Bawendi, J. Seo, *Nature* **2021**, *590*, 587.

[4] Z.-K. Tan, R. S. Moghaddam, M. L. Lai, P. Docampo, R. Higler, F. Deschler, M. Price, A. Sadhanala, L. M. Pazos, D. Credgington, F. Hanusch, T. Bein, H. J. Snaith, R. H. Friend, *Nat. Nanotechnol.* **2014**, *9*, 687.

[5] B. Zhao, S. Bai, V. Kim, R. Lamboll, R. Shivanna, F. Auras, J. M. Richter, L. Yang, L. Dai, M. Alsari, M. Alsari, X.-J. She, L. Liang, J. Zhang, S. Lilliu, P. Gao, H. J. Snaith, J. Wang, N. C. Greenham, R. H. Friend, D. Di, *Nat. Photonics* **2018**, *12*, 783.

[6] Y. Cao, N. Wang, H. Tian, J. Guo, Y. Wei, H. Chen, Y. Miao, W. Zou, K. Pan, Y. He, H. Cao, Y. Ke, M. Xu, Y. Wang, M. Yang, K. Du, Z. Fu, D. Kong, D. Dai, Y. Jin, G. Li, H. Li, Q. Peng, W. Jianpu, W. Huang, *Nature* **2018**, *562*, 249.

[7] K. Lin, J. Xing, L. N. Quan, F. P. G. de Arquer, X. Gong, J. Lu, L. Xie, W. Zhao, D. Zhang, C. Yan, W. Li, X. Liu, Y. Lu, J. Kirman, E. H. Sargent, Q. Xiong, Z. Wei, *Nature* **2018**, *562*, 245.

[8] Q. Zhang, S. T. Ha, X. Liu, T. C. Sum, Q. Xiong, *Nano Lett.* **2014**, *14*, 5995.

[9] B. R. Sutherland, S. Hoogland, M. M. Adachi, C. T. Wong, E. H. Sargent, *ACS Nano* **2014**, *8*, 10947.

[10] P. Brenner, M. Stulz, D. Kapp, T. Abzieher, U. W. Paetzold, A. Quintilla, I. A. Howard, H. Kalt, U. Lemmer, *Appl. Phys. Lett.* **2016**, *109*, 141106.

[11] M. L. De Giorgi, M. Anni, *Appl. Sci.* **2019**, *9*, 4591.

[12] Y. Jia, R. A. Kerner, A. J. Grede, B. P. Rand, N. C. Giebink, *Nat. Photonics* **2017**, *11*, 784.

[13] P. Brenner, O. Bar-On, M. Jakoby, I. Allegro, B. S. Richards, U. W. Paetzold, I. A. Howard, J. Scheuer, U. Lemmer, *Nat. Commun.* **2019**, *10*, 988.

[14] C. Qin, A. S. Sandanayaka, C. Zhao, T. Matsushima, D. Zhang, T. Fujihara, C. Adachi, *Nature* **2020**, *585*, 53.

[15] Q. Shang, M. Li, L. Zhao, D. Chen, S. Zhang, S. Chen, P. Gao, C. Shen, J. Xing, G. Xing, B. Shen, X. Liu, Q. Zhang, *Nano Lett.* **2020**, *20*, 6636.

[16] H. Kim, L. Zhao, J. S. Price, A. J. Grede, K. Roh, A. N. Brigeman, M. Lopez, B. P. Rand, N. C. Giebink, *Nature Commun.* **2018**, *9*, 4893.

[17] C. Cho, T. Antrack, M. Kroll, Q. An, T. R. Bärschneider, A. Fischer, S. Meister, Y. Vaynzof, K. Leo, *Adv. Sci.* **2021**, 2101663.

[18] Q. Liao, K. Hu, H. Zhang, X. Wang, J. Yao, H. Fu, *Adv. Mater.* **2015**, *27*, 3405.

[19] S. Yakunin, L. Protesescu, F. Krieg, M. I. Bodnarchuk, G. Nedelcu, M. Humer, G. De Luca, M. Fiebig, W. Heiss, M. V. Kovalenko, *Nat. Commun.* **2015**, *6*, 8056.

[20] H. Zhu, Y. Fu, F. Meng, X. Wu, Z. Gong, Q. Ding, M. V. Gustafsson, M. T. Trinh, S. Jin, X. Zhu, *Nat. Mater.* **2015**, *14*, 636.

[21] G. L. Whitworth, J. R. Harwell, D. N. Miller, G. J. Hedley, W. Zhang, H. J. Snaith, G. A. Turnbull, I. D. Samuel, *Opt. Express* **2016**, *24*, 23677.

[22] H. Cha, S. Bae, M. Lee, H. Jeon, *Appl. Phys. Lett.* **2016**, *108*, 181104.

[23] S. Chen, K. Roh, J. Lee, W. K. Chong, Y. Lu, N. Mathews, T. C. Sum, A. Nurmikko, *ACS Nano* **2016**, *10*, 3959.

[24] Y. Jia, R. A. Kerner, A. J. Grede, A. N. Brigeman, B. P. Rand, N. C. Giebink, *Nano Lett.* **2016**, *16*, 4624.

[25] H. Cha, S. Bae, H. Jung, M. J. Ko, H. Jeon, *Adv. Opt. Mater.* **2017**, *5*, 1700545.

[26] J. R. Harwell, G. L. Whitworth, G. A. Turnbull, I. D. W. Samuel, *Sci. Rep.* **2017**, *7*, 11727.

[27] F. Mathies, P. Brenner, G. Hernandez-Sosa, I. A. Howard, U. W. Paetzold, U. Lemmer, *Opt. Express* **2018**, *26*, A144.

[28] S. W. Eaton, M. Lai, N. A. Gibson, A. B. Wong, L. Dou, J. Ma, L.-W. Wang, S. R. Leone, P. Yang, *Proc. Natl. Acad. Sci.* **2016**, *113*, 1993.

[29] J. Gong, Y. Wang, S. Liu, P. Zeng, X. Yang, R. Liang, Q. Ou, X. Wu, S. Zhang, *Opt. Express* **2017**, *25*, A1154.

[30] B. Tang, H. Dong, L. Sun, W. Zheng, Q. Wang, F. Sun, X. Jiang, A. Pan, L. Zhang, *ACS Nano* **2017**, *11*, 10681.

[31] T. J. Evans, A. Schlaus, Y. Fu, X. Zhong, T. L. Atallah, M. S. Spencer, L. E. Brus, S. Jin, X.-Y. Zhu, *Adv. Opt. Mater.* **2018**, *6*, 1700982.

[32] N. Pourdavoud, A. Mayer, M. Buchmüller, K. Brinkmann, T. Häger, T. Hu, R. Heiderhoff, I. Shutsko, P. Görrn, Y. Chen, H. Scheer, T. Riedl, *Adv. Mater. Technol.* **2018**, *3*, 1700253.

[33] N. Pourdavoud, T. Haeger, A. Mayer, P. J. Cegielski, A. L. Giesecke, R. Heiderhoff, S. Olthof, S. Zaefferer, I. Shutsko, A. Henkel, B.-K. David, M. Stein, M. Cehovski, O. Charfi, H.-H. Johannes, D. Rogalla, M. C. Lemme, M. Koch, Y. Vaynzof, K. Meerholz, W. Kowalsky, H.-C. Scheer, P. Görrn, T. Riedl, *Adv. Mater.* **2019**, *31*, 1903717.

[34] B. Conings, J. Drijkoningen, N. Gauquelin, A. Babayigit, J. D'Haen, L. D'Olieslaeger, A. Ethirajan, J. Verbeeck, J. Manca, E. Mosconi, F. De Angelis, H. Boyen, *Adv. Mater.* **2015**, *5*, 1500477.

[35] E. J. Juarez-Perez, Z. Hawash, S. R. Raga, L. K. Ono, Y. Qi, *Energy Environ. Sci.* **2016**, *9*, 3406.

[36] M. Kulbak, S. Gupta, N. Kedem, I. Levine, T. Bendikov, G. Hodes, D. Cahen, *J. Phys. Chem. Lett.* **2016**, *7*, 167.

[37] G. Li, K. Chen, Y. Cui, Y. Zhang, Y. Tian, B. Tian, Y. Hao, Y. Wu, H. Zhang, *Adv. Opt. Mater.* **2020**, *8*, 1902012.

[38] Z. Liu, J. Yang, J. Du, Z. Hu, T. Shi, Z. Zhang, Y. Liu, X. Tang, Y. Leng, R. Li, *ACS Nano* **2018**, *12*, 5923.

[39] A. S. Sandanayaka, T. Matsushima, F. Bencheikh, S. Terakawa, W. J. Potscavage Jr, C. Qin, T. Fujihara, K. Goushi, J.-C. Ribierre, C. Adachi, *Appl. Phys. Express* **2019**, *12*, 061010.

[40] H. Kim, K. Roh, J. P. Murphy, L. Zhao, W. B. Gunnarsson, E. Longhi, S. Barlow, S. R. Marder, B. P. Rand, N. C. Giebink, *Adv. Opt. Mater.* **2020**, *8*, 1901297.

[41] M. L. De Giorgi, A. Perulli, N. Yantara, P. P. Boix, M. Anni, *J. Phys. Chem. C* **2017**, *121*, 14772.

[42] L. Zhang, F. Yuan, H. Dong, B. Jiao, W. Zhang, X. Hou, S. Wang, Q. Gong, Z. Wu, *ACS Appl. Mater. Interfaces* **2018**, *10*, 40661.

[43] Y. Liu, J. Wang, L. Zhang, W. Liu, C. Wu, C. Liu, Z. Wu, L. Xiao, Z. Chen, S. Wang, *Opt. Express* **2019**, *27*, 29124.

[44] C. Cho, A. Palatnik, M. Sudzius, R. Grodofzig, F. Nehm, K. Leo, *ACS Appl. Mater. Interfaces* **2020**, *12*, 35242.

[45] G. Heliotis, R. Xia, G. A. Turnbull, P. Andrew, W. L. Barnes, I. D. W. Samuel, D. D. Bradley, *Adv. Funct. Mater.* **2004**, *14*, 91.

[46] E. B. Namdas, M. Tong, P. Ledochowitsch, S. R. Mednick, J. D. Yuen, D. Moses, A. J. Heeger, *Adv. Mater.* **2009**, *21*, 799.

[47] G. Turnbull, P. Andrew, W. L. Barnes, I. Samuel, *Phys. Rev. B* **2003**, *67*, 165107.

[48] S. Brittman, S. Z. Oener, K. Guo, H. Āboliņš, A. F. Koenderink, E. C. Garnett, *J. Mater. Chem. C* **2017**, *5*, 8301.

[49] V. Navarro-Fuster, I. Vragovic, E. M. Calzado, P. G. Boj, J. A. Quintana, J. M. Villalvilla, A. Retolaza, A. Juarros, D. Otaduy, S. Merino, M. A. Díaz-García, *J. Appl. Phys.* **2012**, *112*, 043104.

[50] J. A. Kurvits, M. Jiang, R. Zia, *J. Opt. Soc. Am. A* **2015**, *32*, 2082.